3-2001

Bending Instability in Electrospinning of Nanofibers

A. L. Yarin

S. Koombhongse

Darrell Hyson Reneker
University of Akron Main Campus, reneker@uakron.edu

Bending instability in electrospinning of nanofibers

A. L. Yarin
Faculty of Mechanical Engineering, Technion, Haifa 32000, Israel

S. Koombhongse and D. H. Reneker[a)]
Maurice Morton Institute of Polymer Science, Department of Polymer Science, The University of Akron, Akron, Ohio 44325-3909

A localized approximation was developed to calculate the bending electric force acting on an electrified polymer jet, which is a key element of the electrospinning process for manufacturing of nanofibers. Using this force, a far reaching analogy between the electrically driven bending instability and the aerodynamically driven instability was established. Continuous, quasi-one-dimensional, partial differential equations were derived and used to predict the growth rate of small electrically driven bending perturbations of a liquid column. A discretized form of these equations, that accounts for solvent evaporation and polymer solidification, was used to calculate the jet paths during the course of nonlinear bending instability leading to formation of large loops and resulting in nanofibers. The results of the calculations are compared to the experimental data acquired in the present work. Agreement of theory and experiment is discussed. © *2001 American Institute of Physics.* [DOI: 10.1063/1.1333035]

I. INTRODUCTION

Electrospinning of polymer solutions and melts is a promising process for manufacturing fibers with cross-sectional diameters of about 10^2 nm.[1] Mechanics of this process deserve a special attention, since there is an urgent need for predictive tools to develop deeper understanding and optimization. As was shown in a recent publication of this group,[2] the bending instability of electrified polymer jets plays a central role in the electrospinning process. This relates the electromechanical aspects of the process to the pioneering studies of Taylor[3] of the instabilities of electrified liquid jets of low-molecular mass Newtonian liquids. In particular, Taylor[3] recognized that bending instability can occur, and derived a characteristic equation for small bending perturbations of an inviscid liquid column.

Discretized equations describing the dynamics of the bending instability of electrified jets of polymer solutions were proposed and solved in Ref. 2. In the present work we elucidate the relation of these equations to the quasi-one-dimensional partial differential equations of the dynamics of thin free liquid jets. The latter were proposed and used mainly in the studies of the aerodynamically driven bending instability of liquid jets moving in air with high enough speed.[4,5] The main difference between the electrically and aerodynamically driven instabilities is in the nature of the destabilizing force. In Sec. II of the present work we introduce a localized approximation leading to a very simple expression for the bending force acting on the jet due to mutual Coulomb interactions. Using this force, in Sec. III we formulate the continuous quasi-one-dimensional partial differential equations of the dynamics of bending electrified jets. We

also show how these equations correspond to the discretized equations used in Ref. 2.

In Sec. IV we present the expressions for the growth rate and the wavelength of small electrically driven bending perturbations of an electrified liquid column. In Sec. V solvent evaporation and the related solidification processes are accounted for. Examples of calculations are shown, discussed and compared with experiment in Sec. VI. Conclusions are drawn in Sec. VII.

II. LOCALIZED APPROXIMATION

In the dynamics of thin vortices in fluids the localized-induction approximation is widely used to describe velocity induced at a given vortex element by the rest of the vortex line.[6–10] A similar approach may be used to calculate the electric force imposed on a given element of an electrified jet by the rest of it. Consider an enlarged element of a curved jet shown in Fig. 1. We assume that the arc length ξ is reckoned along the jet axis from the central cross section of the element where $\xi=0$. We denote the coordinates reckoned along the normal and binormal by y and z, so that the radius vector of point A on the surface of the element $\mathbf{R}_{OA}=y\mathbf{n}+z\mathbf{b}$. The radius vector of point B at the jet axis close enough to the element considered is thus given by

$$\mathbf{R}_{OB}=\boldsymbol{\tau}\xi+\tfrac{1}{2}|k_0|\xi^2\mathbf{n}, \tag{1}$$

where k_0 is the curvature of the jet axis at point O and τ is a unit tangent vector. Therefore

$$\mathbf{R}_{BA}=\mathbf{R}_{OA}-\mathbf{R}_{OB}=[y-\tfrac{1}{2}|k_0|\xi^2]\mathbf{n}+z\mathbf{b}-\boldsymbol{\tau}\xi. \tag{2}$$

Denote the cross-sectional radius of the jet element by a, assume that charge is uniformly distributed over the jet surface with the surface density Δe, and denote the charge per

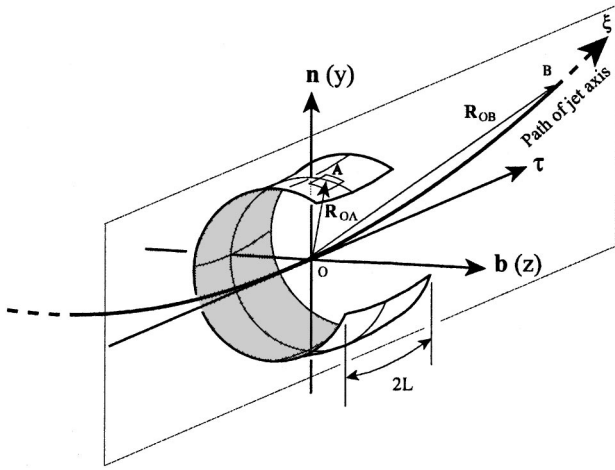a)Electronic mail: dhr@polymer.uakron.edu

FIG. 1. Sketch of an enlarged element of a curved jet and the associated normal, binormal and tangent vectors **n**, **b**, and $\boldsymbol{\tau}$.

unit jet length by $e = 2\pi a \Delta e$. Then the Coulomb force acting at a surface element near point A from the jet element situated near point B is given by

$$d\mathbf{F}_{BA} = \frac{e \, d\xi \cdot \Delta e \cdot a \, d\theta \, d\xi}{|\mathbf{R}_{BA}|^3} \mathbf{R}_{BA}, \qquad (3)$$

where θ is the polar angle in the jet cross section.
Substituting Eq. (2) in Eq. (3) and accounting for the fact that $y = a \cos\theta$, and $z = a \sin\theta$, we obtain from Eq. (3)

$$d\mathbf{F}_{BA} = e \, d\xi \Delta e \cdot a$$
$$\times d\theta d\xi \frac{[(a\cos\theta - |k_0|\xi^2/2)\mathbf{n} + a\sin\theta\mathbf{b} - \boldsymbol{\tau}\xi]}{[a^2 - a\cos\theta|k_0|\xi^2 + |k_0|^2\xi^4/4 + \xi^2]^{3/2}}. \qquad (4)$$

For a thin jet, as $a \to 0$, all the terms containing a in the numerator of Eq. (4) can be safely neglected, also in the denominator the term $a \cdot \cos\theta|k_0|\xi^2$ is negligibly small as compared to ξ^2. Then using Eq. (4) we calculate the electric force acting on a particular element of the jet, assuming that the length of the element is $2L$, with L being a cutoff for the integral, to be determined later on

$$\mathbf{F}_{el} = \int_0^{2\pi} d\theta \int_{-L}^{L} d\mathbf{F}_{AB}$$
$$= e^2 d\xi \int_{-L}^{L} d\xi \frac{-\boldsymbol{\tau}\xi - |k_0|\xi^2\mathbf{n}/2}{[a^2 + \xi^2 + |k_0|^2\xi^4/4]^{3/4}}. \qquad (5)$$

The latter yields

$$\mathbf{F}_{el} = e^2 d\xi \int_{-L/a}^{L/a} dx \left[\frac{-\boldsymbol{\tau}x}{a(1+x^2)^{3/2}} - \frac{|k_0|x^2\mathbf{n}/2}{(1+x^2)^{3/2}} \right]. \qquad (6)$$

The force in the axial direction obviously cancels, whereas the force becomes

$$\mathbf{F}_{el} = -e^2 ln\left(\frac{L}{a}\right)|k|\mathbf{n} d\xi. \qquad (7)$$

This shows that the net electric force acting on a jet element is related to its curvature $k = k_0$, and acts in the normal (lat-

eral) direction to the jet axis. The magnitude of the net force acting on a jet element due to the action of the surface tension forces is equal to

$$\mathbf{F} = \pi a \sigma \boldsymbol{\tau}|_{\xi + d\xi} - \pi a \sigma \boldsymbol{\tau}|_{\xi} = \pi a \sigma |k|\mathbf{n} d\xi, \qquad (8)$$

where σ is the surface tension coefficient.
Therefore, the net normal (lateral) force acting on a jet element is given by the sum of the electric and surface tension forces, Eqs. (7) and (8), as

$$d\mathbf{F} = |k|\mathbf{n} d\xi\left[\pi a \sigma - e^2 ln\frac{L}{a} \right]. \qquad (9)$$

The cutoff length L is still to be found. It will be done below in Sec. IV.

III. CONTINUOUS QUASI-ONE-DIMENSIONAL EQUATIONS OF THE DYNAMICS OF ELECTRIFIED LIQUID JETS

For very thin jets we can neglect, in the first approximation, the effect of the shearing force in the jet cross section, as well as the bending stiffness (Ref. 5, p. 49). If we use a Lagrangian parameter s "frozen" into the jet elements, then the momentless quasi-one-dimensional equations of the jet dynamics (Ref. 5, Eq. (4.19) p. 49) take the form

$$\lambda f = \lambda_0 f_0, \qquad (10a)$$

$$\rho\lambda_0 f_0 \frac{\partial \mathbf{V}}{\partial t} = \boldsymbol{\tau}\frac{\partial P}{\partial s} + \lambda|k|P\mathbf{n} - \rho g\lambda_0 f_0\mathbf{k} + \lambda|k|$$
$$\times\left(\pi a \sigma - e^2 ln\frac{L}{a} \right)\mathbf{n} - \lambda e\frac{U_0}{h}\mathbf{k}. \qquad (10b)$$

Equation (10a) is the continuity equation with λ being the geometrical stretching ratio, so that $\lambda ds = d\xi$, and $f = \pi a^2$ the cross-sectional area. Subscript zero denotes the parameter values at time $t = 0$. Equation (10b) is the momentum balance equation with ρ being the liquid density, $\mathbf{V}$ its velocity, P the longitudinal force in the jet cross section (of viscoelastic origin in the case of electrospinning of polymer jets), $g\mathbf{k}$ gravity acceleration, U_0/h the outer field strength (the outer field is assumed to be parallel to the unit vector $\mathbf{k}$, with U_0 being the value of electrical potential at the jet origin, and h the distance between the origin and a ground plate). It is emphasized that on the right-hand side of the momentum Eq. (10b) we account for the longitudinal internal force of rheological origin acting on the jet (the first two terms), the gravity force (the third term), the bending electrical force and the stabilizing effect of the surface tension [the fourth term following from Eq. (9)], and for the electric force acting on the jet from electric field created by the potential difference of the starting point of the jet and the collector.
Equations (10) are supplemented by the kinematic relation

$$\frac{\partial \mathbf{R}}{\partial t} = \mathbf{V}, \qquad (11)$$

where $\mathbf{R}$ is the radius vector of a point on the axis of the jet.

Introducing the Cartesian coordinate system associated with a capillary (the jet origin) or a ground plate, with unit vectors **i**, **j**, and **k**, and accounting for

$$\mathbf{R}=\mathbf{i}X+\mathbf{j}Y+\mathbf{k}Z, \tag{12a}$$

$$\mathbf{V}=\mathbf{i}u+\mathbf{j}v+\mathbf{k}w, \tag{12b}$$

we obtain from the projections of (10b) and (11) the following system of scalar equations:

$$\rho\lambda_0 f_0 \frac{\partial u}{\partial t}=\tau_X\frac{\partial P}{\partial s}+\lambda|k|Pn_X+\lambda|k|$$
$$\times\left(\pi a\sigma-e^2 ln\frac{L}{a}\right)n_X, \tag{13a}$$

$$\rho\lambda_0 f_0 \frac{\partial v}{\partial t}=\tau_Y\frac{\partial P}{\partial s}+\lambda|k|Pn_Y+\lambda|k|$$
$$\times\left(\pi a\sigma-e^2 ln\frac{L}{a}\right)n_Y, \tag{13b}$$

$$\rho\lambda_0 f_0 \frac{\partial w}{\partial t}=\tau_Z\frac{\partial P}{\partial s}+\lambda|k|Pn_Z+\lambda|k|$$
$$\times\left(\pi a\sigma-e^2 ln\frac{L}{a}\right)n_Z-\rho g\lambda_0 f_0-\lambda e\frac{U_0}{h}, \tag{13c}$$

$$\frac{\partial X}{\partial t}=u, \tag{13d}$$

$$\frac{\partial Y}{\partial t}=v, \tag{13e}$$

$$\frac{\partial Z}{\partial t}=w. \tag{13f}$$

The following geometric relations should be added:

$$\lambda=(X_{,s}^2+Y_{,s}^2+Z_{,s}^2)^{1/2}, \tag{14a}$$

$$\tau_X=\frac{1}{\lambda}\frac{\partial X}{\partial s}, \tag{14b}$$

$$\tau_Y=\frac{1}{\lambda}\frac{\partial Y}{\partial s}, \tag{14c}$$

$$\tau_Z=\frac{1}{\lambda}\frac{\partial Z}{\partial s}, \tag{14d}$$

$$n_X=\frac{1}{|k|\lambda}\frac{\partial\tau_X}{\partial s}, \tag{14e}$$

$$n_Y=\frac{1}{|k|\lambda}\frac{\partial\tau_Y}{\partial s}, \tag{14f}$$

$$n_Z=\frac{1}{|k|\lambda}\frac{\partial\tau_Z}{\partial s}, \tag{14g}$$

$$|k|=\left[\frac{(X_{,s}^2+Y_{,s}^2+Z_{,s}^2)(X_{,ss}^2+Y_{,ss}^2+Z_{,ss}^2)-(X_{,s}X_{,ss}+Y_{,s}Y_{,ss}+Z_{,s}Z_{,ss})^2}{(X_{,s}^2+Y_{,s}^2+Z_{,s}^2)^3}\right]^{1/2}. \tag{14h}$$

Also assuming the simplest version of the upper-convected Maxwell model of viscoelasticity properly fitted to describe uniaxial elongation,[2,5] we obtain the equation for the normal stress in the jet cross-section $\sigma_{\tau\tau}$

$$\frac{\partial\sigma_{\tau\tau}}{\partial t}=G\frac{1}{\lambda}\frac{\partial\lambda}{\partial t}-\frac{G}{\mu}\sigma_{\tau\tau}, \tag{15}$$

where G is the modulus of elasticity, and μ the viscosity, and

$$\frac{1}{\lambda}\frac{\partial\lambda}{\partial t}=\frac{X_{,s}u_{,s}+Y_{,s}v_{,s}+Z_{,s}w_{,s}}{\lambda^2}. \tag{16}$$

Then the longitudinal force P is given by

$$P=\frac{\lambda_0 f_0}{\lambda}\sigma_{\tau\tau}. \tag{17}$$

It is emphasized that in Eq. (17) there actually should stand the normal stress difference $\sigma_{\tau\tau}-\sigma_{nn}$ instead of $\sigma_{\tau\tau}$. However, in strong uniaxial elongational flows (electrospinning is an example of such flow) the axial component $\sigma_{\tau\tau}\gg\sigma_{nn}$, and the latter can be neglected. A detailed proof of this fact

can be found in Ref. 11.

Also the equation of the charge conservation in a jet element holds

$$e\lambda=e_0\lambda_0. \tag{18}$$

The system of the equations presented in this section allows one to find the jet configuration in space at any moment of time. It is emphasized that the equations used in Ref. 2 to calculate the jet evolution in electrospinning represent a discretized form of those presented here. In Ref. 2 the equations were derived considering the jet to be a locus of inertial electrically charged beads connected by the spring and dashpot viscoelastic elements. The only difference is in the fact that here the bending electric force is calculated using the localized approximation with an appropriate cutoff of the integral (cf. Sec. II), whereas in Ref. 2 the whole integral responsible for the electric force was accounted for in the discretized form.

IV. GROWTH RATE AND WAVELENGTH OF SMALL BENDING PERTURBATIONS OF ELECTRIFIED LIQUID COLUMN

In Refs. 4 and 5 the theory of the aerodynamically driven jet bending was described. In that case, due to the jet curvature, a distributed lift force acts on the jet (as a consequence of the Bernoulli equation for air flow), which enhances perturbations and makes the perturbations grow. The aerodynamic bending force per jet length $d\xi$ in the case of small bending perturbations is given by[4,5]

$$\mathbf{F}_{aer} = -\rho_a V_0^2 \pi a_0^2 |k| \mathbf{n} d\xi, \tag{19}$$

where ρ_a is the air density, V_0 is the jet velocity, and a_0 the jet cross-sectional radius which does not change for small perturbations.

This force is the only difference between the aerodynamic-and electric-driven bending. Comparing Eq. (7) (with $e = e_0$) with Eq. (19), we see that all the results obtained in Refs. 4 and 5 for the aerodynamic bending may also be used here in the case of electric bending, if one replaces the factor $\rho_a V_0^2$ by $e_0^2 ln(L/a_0)/\pi a_0^2$.

Dynamics of small bending perturbations was studied in Refs. 4 and 5 accounting for the shearing force and moment in jet cross section [thus, accounting for the bending stiffness in the equations generalizing Eq. (13)]. For example, the case of viscous Newtonian fluid was considered. We recast these results here for the case of an electrified liquid column of Newtonian fluid of viscosity μ. This, in particular, generalizes the results of Taylor[3] to the viscous case, and allows us to find the cutoff length L.

Recasting the results of Refs. 4 and 5, we find that the destabilizing electric force overcomes the stabilizing effect of the surface tension if

$$e_0^2 ln\left(\frac{L}{a_0}\right) > \pi a_0 \sigma. \tag{20}$$

If we assume $a_0 = 0.015$ cm, and the jet charge of 1 Coulomb/l, then $e_0 = 2120.5 \, (g \, cm)^{1/2}/s$. Below we show that a reasonable value of L is $L = 0.0325$ cm. Using it for the estimate, we find that $e_0^2 ln(L/a_0) = 3.465 \times 10^6$ g cm/s^2, whereas $\pi a_0 \sigma = 3.3$ g cm/s^2 for $\sigma = 70$ g/s^2. Therefore, in this case the inequality (20) definitely holds and the bending instability should set in and grow.

From the results of Refs. 4 and 5 we obtain in the present case that the wave number χ_* and the growth rate γ_* of the fastest growing bending perturbation are given by

$$\chi_* = \left\{ \frac{8}{9} \frac{\rho a_0^2}{\mu^2} \left[\frac{e_0^2 ln(L/a_0)}{\pi a_0^2} - \frac{\sigma}{a_0} \right] \right\}^{1/6}, \tag{21a}$$

$$\gamma_* = \frac{[e_0^2 ln(L/a_0)/\pi a_0 - \sigma]^{2/3}}{(3\mu\rho a_0^4)^{1/3}}. \tag{21b}$$

Here $\chi_* = 2\pi a_0/l_*$, where l_* is the wavelength of the fastest growing perturbation.

The results (21) correspond to the maximum of the spectrum $\gamma(\chi)$ given by the characteristic equation

$$\gamma^2 + \frac{3}{4} \frac{\mu \chi^4}{\rho a_0^2} \gamma + \left[\frac{\sigma}{\rho a_0^3} - \frac{e_0^2 ln(L/a_0)}{\pi \rho a_0^4} \right] \chi^2 = 0. \tag{22}$$

This equation is to be compared with the characteristic equation for electrically driven bending perturbations of an inviscid liquid ($\mu = 0$) column derived by Taylor[3] [his Eq. (12)]. Expanding that equation in the long-wave limit as $\chi \to 0$, we find that it reduces to Eq. (22) with the term $ln(1/\chi_*)$ instead of $ln(L/a_0)$. This fact defines the cutoff length L, since the result of Taylor[3] is exact. Thus taking $ln(L/a_0) = ln(1/\chi_*)$ and neglecting the minor surface tension effect in Eq. (21a), we reduce the latter to the form

$$\chi_* = \left[\frac{8}{9} \frac{\rho}{\mu^2} \frac{e_0^2}{\pi} ln\left(\frac{1}{\chi_*} \right) \right]^{1/6}, \tag{23}$$

which is the equation defining χ_* (and thus, L). Taking the same values of the parameters as before, as well as $\rho = 1$ g/cm^3 and $\mu = 10^4$ g/(cm s) (remind that $e_0 = 2120.5 \, (g \, cm)^{1/2}/s$), we reduce Eq. (23) to the form

$$\chi_* = 0.483 \left[ln\left(\frac{1}{\chi_*} \right) \right]^{1/6}, \tag{24}$$

which yields $\chi_* = 0.462$.

Therefore the wavelength of the fastest growing perturbation $l_* = 2\pi \cdot 0.015/0.462 = 0.204$ cm, and the cutoff length $L = l_*/2\pi = 0.0325$ cm. Comparing the latter with the jet cross-sectional radius $a_0 = 0.015$ cm, we see that the cutoff length is very short, of the order of a_0.

Based on the results of Refs. 4 and 5, it also follows that the bending perturbations of highly viscous liquids grow much faster than the capillary ones (driven by the surface tension), if the condition

$$\frac{\pi\mu^2}{\rho e_0^2 ln(L/a_0)} \gg 1 \tag{25}$$

is fulfilled.
For the values of the parameters used in the present section, the left-hand side of Eq. (25) is equal to 90.7, which shows that the inequality (25), indeed, holds. Therefore such a jet bends with a nearly constant radius.

V. EVAPORATION AND SOLIDIFICATION

In Ref. 2 calculations of the bending polymer jets in the electrospinning process were done neglecting evaporation and solidification effects. We account for them in the present work.

In Ref. 12 the following correlation is given for the Nusselt number for a cylinder moving parallel to its axis in air:

$$Nu = 0.42 \, Re^{1/3}, \tag{26}$$

where the Reynolds number $Re = V2a/\nu_a$, a is the cross-sectional radius, and ν_a the kinematic viscosity of air. The Nusselt number is the dimensionless heat transfer coefficient describing heat transfer rate.

Taking the Prandtl number of air to be $Pr = 0.72$, we can generalize the correlation (26) for an arbitrary value of the Prandtl number as

$$Nu = 0.495 \cdot Re^{1/3} Pr^{1/2}. \tag{27}$$

Similarly to (27), we take the following correlation for the Sherwood number:

$$\text{Sh}=0.495\cdot\text{Re}^{1/3}\cdot\text{Sc}^{1/2}, \qquad (28)$$

where $\text{Sh}=h_m 2a/D_a$, where h_m is the mass transfer coefficient for evaporation, D_a is the vapor diffusion coefficient in air, and the Schmidt number $\text{Sc}=\nu_a/D_a$. The Sherwood number is the dimensionless mass transfer coefficient describing the evaporation rate.

Correlations of the type of Eqs. (26)–(28) are valid for air ($\text{Pr}=0.72$) for Reynolds number in the range $1\leq\text{Re}\leq 60$. For $a\leq 10^{-2}$ cm, $V\sim 10^2-10^3$ cm/s and $\nu_a=0.15$ cm^2/s, the Reynolds number is $10\leq\text{Re}\leq 10^2$ which corresponds approximately to the range of validity.

The initial mass of polymer in a jet element is given by

$$M_{p0}=\rho f_0\lambda_0 ds\cdot c_{p0}, \qquad (29)$$

where c_{p0} is the initial polymer mass fraction. The variable solvent content in the element is

$$M_s=\rho f\lambda ds-\rho f_0\lambda_0 ds\cdot c_{p0}, \qquad (30)$$

which corresponds to the solvent mass fraction

$$c_s=1-\frac{f_0\lambda_0}{f\lambda}c_{p0}. \qquad (31)$$

The solvent mass decreases due to evaporation according to the equation

$$\frac{\partial M_s}{\partial t}=-\rho h_m[c_{s,\text{eq}}(T)-c_{s\infty}]2\pi a\lambda ds, \qquad (32)$$

where $c_{s,\text{eq}}(T)$ is the saturation vapor concentration of solvent at temperature T, and $c_{s\infty}$ is the vapor concentration in atmosphere far from the jet.

For water as a solvent, Ref. 13, for example, recommends the following expression for $c_{s,\text{eq}}(T)$:

$$c_{s,\text{eq}}=\frac{1}{1013}\{a_0+T[a_1+T(a_2+T(a_3+T(a_4+T$$

$$\times(a_5+a_6T))))]\}, \qquad (33)$$

$a_0=6.107799961,$
$a_1=4.436518521\times10^{-1},$
$a_2=1.428945805\times10^{-2},$
$a_3=2.650648731\times10^{-4},$
$a_4=3.031240396\times10^{-6},$
$a_5=2.034080948\times10^{-8},$
$a_6=6.136820929\times10^{-11},$

where T is taken in degrees Celsius. Concentration $c_{s\infty}$ is equal to a relative humidity in atmosphere.

Substituting Eqs. (28) and (30) in Eq. (32), we obtain the equation describing variation of the jet volume

$$\frac{\partial f\lambda}{\partial t}=-D_a\cdot 0.495\cdot\text{Re}^{1/3}\text{Sc}^{1/2}[c_{s,\text{eq}}(T)-c_{s\infty}]\pi\lambda. \qquad (34)$$

Solvent mass decreases until the solvent mass ratio defined by Eq. (32) becomes small enough (say, $c_s=0.1$), at which point the evaporation part of the calculation is stopped and viscosity remains at a constant value. This cutoff can be rationalized by the assumption that further evaporation is reduced because the diffusion coefficient of solvent in the remaining polymer is small.

When evaporation is accounted for as per Eq. (34), the left-hand sides of the equations (10b), and (13a)–(13c) become, respectively

$$\rho\frac{\partial f\lambda\mathbf{V}}{\partial t}, \qquad (35a)$$

$$\rho\frac{\partial f\lambda u}{\partial t}, \qquad (35b)$$

$$\rho\frac{\partial f\lambda v}{\partial t}, \qquad (35c)$$

$$\rho\frac{\partial f\lambda w}{\partial t}. \qquad (35d)$$

Also the gravity term in (13c) should contain $f\lambda$ instead of $f_0\lambda_0$, since due to evaporation $f\lambda$ is not equal to $f_0\lambda_0$ anymore.

If the discretized version[2] of the model is used, λ in Eq. (34) is replaced by the distance between two adjoining beads.

The local polymer mass ratio in the jet is given by

$$c_p=c_{p0}\frac{f_0\lambda_0}{f\lambda}. \qquad (36)$$

We account for the solidification process due to solvent evaporation by employing the following correlation for the viscosity dependence on polymer concentration:[12]

$$\mu=10^A\times10^{Bc_p^m} \qquad (37)$$

with $m=0.1-1$.

The value of the parameter B is estimated as follows. According to Ref. 12 (p. 32), when c_p is doubled, viscosity of the solution increases by a factor in the range of $10-10^2$. Using the value 10^2 and assuming that c_p increased from 0.1 to 0.2, we find for $m=1$ that $B=20$. The value of $B=17.54$ corresponds to the factor of 10 and $m=0.1$. Therefore the order of magnitude estimate of B yields the value $B=O(10)$. The value of A is unimportant, since the initial value of the viscosity $\mu_0=10^A\times10^{Bc_{p0}^m}$ is assumed to be known and is used for scaling. On the other hand, the relaxation time θ is proportional to c_p (Ref. 5). Therefore

$$\frac{\theta}{\theta_0}=\frac{c_p}{c_{p0}}, \qquad (38)$$

where the initial relaxation time in known.

The modulus of elasticity is $G=\mu/\theta$. Rendering the equations of the problem dimensionless as in Ref. 2, we obtain the rheological constitutive Eq. (15) in the following dimensionless form:

$$\frac{\partial\bar{\sigma}_{\tau\tau}}{\partial\bar{t}}=\bar{G}\frac{\partial\lambda}{\lambda\partial\bar{t}}-\frac{\bar{G}}{\bar{\mu}}\bar{\sigma}_{\tau\tau}. \qquad (39)$$

Here G is rendered dimensionless by $G_0 = \mu_0 / \theta_0$, and μ by μ_0. Therefore

$$\bar{G} = \frac{10^{B(c_p^m - c_{p0}^m)}}{c_p / c_{p0}}, \tag{40}$$

$$\bar{\mu} = 10^{B(c_p^m - c_{p0}^m)} \tag{41}$$

with $B = O(10)$.

All the dimensionless groups introduced in Ref. 2 contain now μ_0 and G_0. Two new dimensionless groups appear: the Deborah number

$$\text{De} = \frac{\mu_0 / G_0}{a_0^2 / D_a} \tag{42}$$

representing the ratio of the relaxation time $\theta_0 = \mu_0 / G_0$ to the diffusional characteristic time a_0^2 / D_a, and

$$\delta = \frac{L_{el} a_0}{(\mu_0 / G_0) \nu_a}. \tag{43}$$

The latter is based on the ''electric'' characteristic length L_{el} introduced in Ref. 2. The group δ is involved in the calculation of the Reynolds number Re. The model of Ref. 2 updated to account for solvent evaporation was used for the calculations in the present work.

VI. RESULTS AND DISCUSSION

A. Jet path calculated for the electrically driven bending instability accounting for evaporation and solidification

As was shown in Ref. 2 the qualitative pattern of the jet behavior in the electrospinning process can be drawn without accounting for evaporation and solidification. Only a quantitative comparison can be made for the solidification. Such a comparison is the aim of the present section. Also, a comparison between the results obtained with and without account for evaporation and solidification will be made here.

Calculations of the present work were done for an aqueous solution with initial 6% concentration of poly(ethylene oxide) studied experimentally in Ref. 2, as well as in the present work. In Ref. 2 the following values of the dimensional parameters were established: the initial cross-sectional radius $a_0 = 150 \, \mu$m, the density $\rho = 10^3 \, \text{kg/m}^3$, the surface tension $\sigma = 0.07 \, \text{kg/s}^2$, the initial viscosity $\mu_0 = 10^3 \, \text{kg/(m s)}$, the initial relaxation time $\theta_0 = 10 \, \text{ms}$, the charge density $1 \, C/l$, the distance to the collecting plate $h = 20 \, \text{cm}$. In the calculations of the present work we took the field strength $U_0 / h = 1.5 \, \text{kV/m}$. In the experiment, the electric field was $50 \, \text{kV/m}$. The values of the dimensionless groups introduced in Ref. 2 are now based on the initial values of the dimensional parameters and are equal to $Q = F_{ve} = 78 \, 359.57$, $V = 47.02$, $A = 17.19$, $K_S = 100$ and $H = 626.88$, whereas $L_{el} = 0.319 \, \text{cm}$. We also take a humidity of 16.5%, $c_{s\infty} = 0.165$, and a temperature of 20 °C. The best representation of the envelope cone of the bending loops (see below) was found at $B = 7$ and $m = 0.1$ in the solidification law (37), (40) and (41), which agrees with the estimates known from literature and those discussed in the previous section. These values were used in the present calculations.
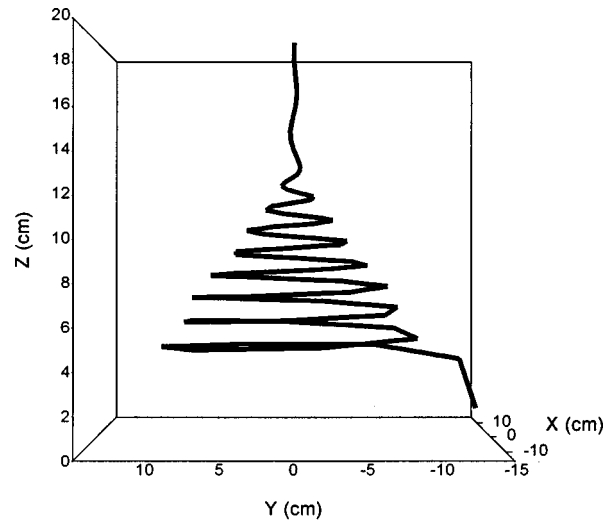
(a)
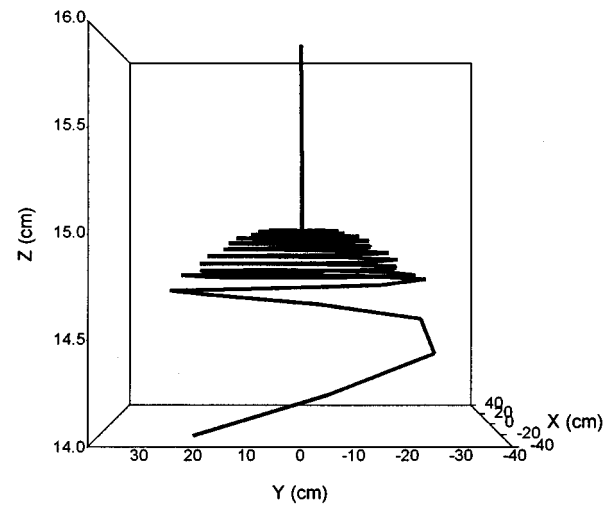
(b)

FIG. 2. (a) Jet path calculated accounting for evaporation and solidification. (b) Jet path calculated without accounting for evaporation and solidification.

Figure 2(a) shows the path of the jet calculated accounting for evaporation and solidification, whereas Fig. 2(b) was calculated without accounting for these effects. Due to evaporation and solidification each loop of the jet becomes more viscous with time, and its elastic modulus increases. As a result, the bending stiffness increases, and the radius of the bending loops in Fig. 2(a) (with evaporation and solidification) is smaller than that of Fig. 2(b) (without evaporation and solidification). The radius of the bending perturbations of the jet calculated accounting for the evaporation and solidification effects is comparable with that found in the experiment (cf. Fig. 3), which is illustrated in the following subsection.

B. Envelope cone

Shape of the envelope cone can be easily seen by a naked eye, or using a camera with long exposure time (cf. Fig.

FIG. 3. Image of the electrically driven bending instability taken near the end of the straight part of the jet in experiment.

4). The two bright lines bifurcating in Fig. 4 from a point emphasized by the arrow resulted from specular reflection of light from segments near the maximum lateral excursion of each loop. Each loop moved downward during the long exposure time of the camera and created the bright lines seen in Fig. 4, which define the envelope cone of the bending jet during the electrospinning process. For comparison with the results of the calculations, the generatrix of the envelope cone in Fig. 4 is also represented in Fig. 5.
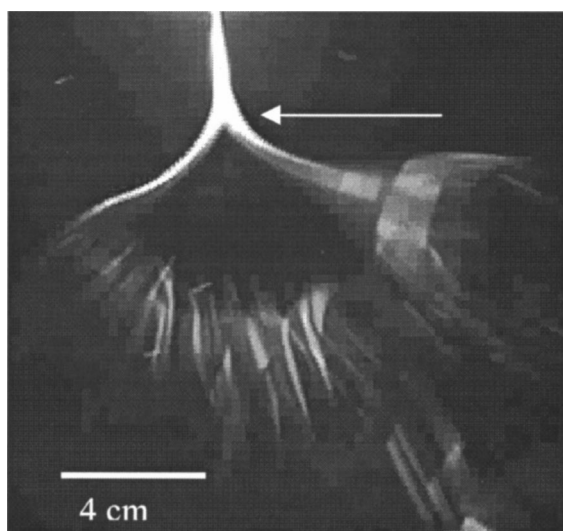

FIG. 4. Shape of the envelope cone created by the electrically driven bending instability. The complicated image in the lower part of the figure is a consequence of the long exposure time (~16 ms) used to observe the envelope cone, and the time varying path of the jet in that region.
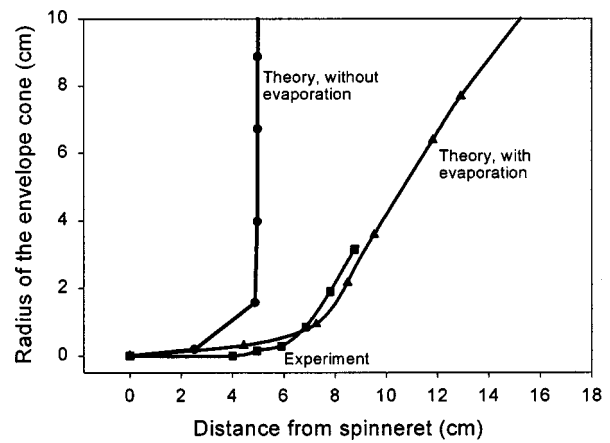

FIG. 5. Shape of the envelope cone: experiment vs theory. Points show calculated radii of successive loops. Experimental points were measured from a photograph.

The calculations showed that evaporation and solidification have a strong effect on the predicted shape of the envelope cone. Two theoretical curves: without evaporation and solidification, and with this effect accounted for ($m=0.1$) are presented in Fig. 5. It is clearly seen that the result accounting for evaporation and solidification agrees fairly well with the experimental data.

The envelope visible in the experiment does not extend beyond a radius of about 3 cm, whereas the theory allowed for the further growth of radius until 10 cm. The reason may be that after the jet had solidified in the experiment, it became much more rigid, i.e., unstretchable. On the other hand, in the theoretical calculations the solidified jet is still described as a liquid (albeit highly viscous, with a high elastic modulus), which still allows for some additional stretching. Actually, the comparison in Fig. 5 shows that the calculations should be stopped as the radius of the envelope cone has achieved the value of 3–4 cm.

C. Jet velocity

Downward velocity in the electrified jet was measured by following the downward motion of a loop. The compari-
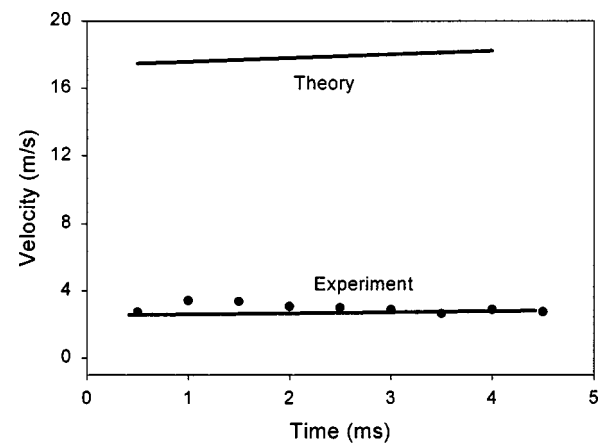

FIG. 6. Downward velocity of the jet: experiment vs theory. $B=7$, $m=0.1$.
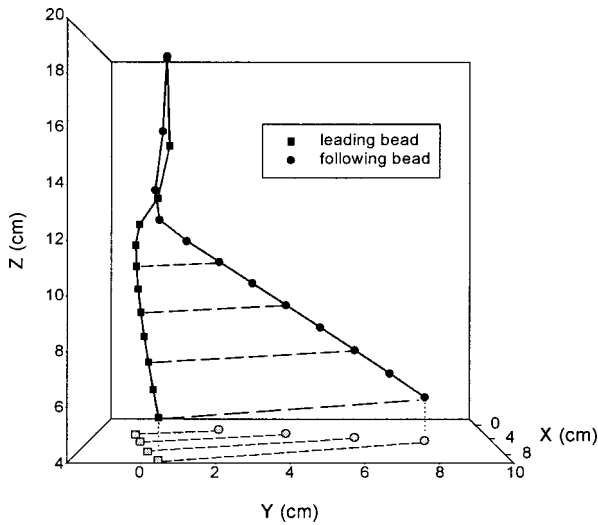
FIG. 7. Stretching of a segment of the jet. Each solid line represents a trajectory of one of the two successive beads. The dashed lines represent the segment of the jet between the successive beads. The length of the segment increases with time as a result of the jet stretching during the course of electrospinning. $B = 7$, $m = 0.1$. The projection of the bead positions onto the X-Y plane are shown by the gray symbols.

FIG. 9. Calculated viscosity along the jet; $t = 6$ ms, $B = 7$ and $m = 0.1$. The calculated radius of the envelope cone continued to grow after the viscosity reached the plateau.

son of the experimental and theoretical results is shown in Fig. 6. The velocity is practically independent of time in both experiment and theory. The theoretical value of the velocity overestimates the measured value by a factor of 4. Given the fact that the values of several governing parameters used in the experiments are only order of magnitude estimates, the discrepancy represented by the factor of 4 is not dramatic. Comparing the results shown in Fig. 6 with those shown in Fig. 18 in Ref. 2, we can conclude that accounting for the evaporation and solidification improves the trend of the predictions. In the present work the downward velocity is almost constant, as in the experiment, whereas in Ref. 2 (without evaporation and solidification) it was increasing with time. It should be noted that direct comparison with the result of Ref. 2 is impossible since some of the governing parameters were different.

D. Elongation and drying of the jet

The theoretical results suggest that stretching of material elements along the jet makes it possible to achieve very high draw ratio values in the electrospinning process. In the calculation the initial distance between two successive beads was 3.99×10^{-4} cm, whereas the final distance between the same two beads was 13.92 cm. Assuming that the initial polymer concentration in the jet was 6%, the cross-sectional radius of a dry fiber (a_f) after elongation and solvent evaporation have been completed is related to the initial radius of the jet (a_0) by the material balance equation

$$\pi a_f^2 \cdot 13.92 = \pi a_0^2 \cdot 3.99 \cdot 10^{-4} \cdot 0.06. \tag{44}$$

For $a_0 = 150 \, \mu$m this yields $a_f = 196.7$ nm. The corresponding draw ratio due to elongation (cf. Ref. 2) is equal to $(a_0/a_f)^2 \cdot 0.06 = 34815$.

Figure 7 shows the calculated trajectories of two successive beads of the jet in the course of electrospinning. The trajectories are shown by solid lines, and the positions of the beads by black squares and circles. The lines that have longer dashes connect the positions of the adjacent beads. To simplify, not every connection is shown. The projections of the dashed line onto X-Y plane are shown by the lines with shorter dashes. The X-Y projection of the bead positions are shown by gray squares or circles. The dashed lines connecting the two beads at a given time represent the elongating segment. Its increase in length illustrates stretching of the jet element between the two beads. The initial distance between the beads was 3.99×10^{-4} cm, as mentioned above. The time interval covered by Fig. 7 is 6.5 ms. The corresponding draw ratio is shown in Fig. 8 versus the vertical distance of the segment from the tip. It is instructive to see the envelope cone, too (the dashed line in Fig. 8), since it shows where the draw ratio grows. Along the straight part of the jet, which is about 6 cm long, the draw ratio achieves a value of about 1000. In the bending loops inside the envelope cone the draw ratio increases, by another factor of 25, to the value of 25 000. Without evaporation and solidification in the model, the draw ratio extracted from the calculation in Ref. 2 increased very rapidly, as shown in Fig. 8.
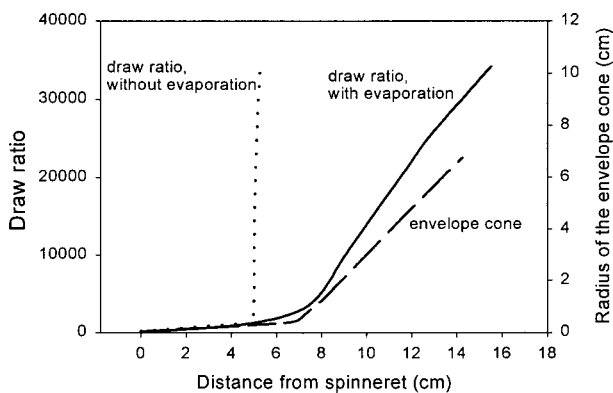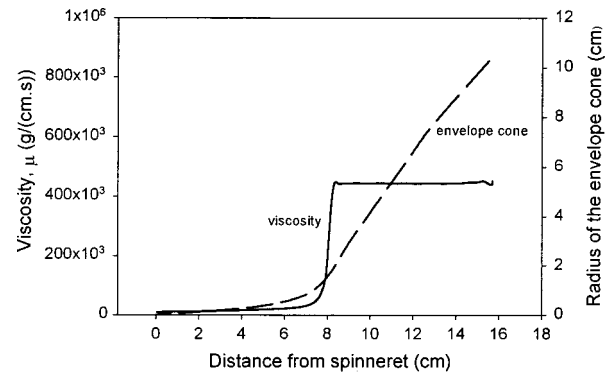

FIG. 8. Calculated draw ratio of a segment of the jet along its length. $B = 7$, $m = 0.1$. The dotted line was generated using the results from Ref. 2.

E. Viscosity profile in the bending jet

The distribution of the viscosity along the jet at t = 6 ms is shown by the solid line in Fig. 9. Viscosity slowly increases along the straight part of the jet. When bending perturbations begin to grow rapidly, velocity of the motion increases, and the evaporation process strongly intensifies. It is clearly seen when comparing the viscosity profile with that of the envelope cone shown in Fig. 9 by the dashed line. Fast evaporation strongly increases the polymer fraction in the jet, which leads to solidification manifested by the appearance of the high viscosity plateau at a distance of about 2 cm from the beginning of the envelope cone. The calculation showed that at the beginning of the viscosity plateau, nanofibers have already been formed, since the cross-sectional radius of the fiber is already reduced to about 640 nm.

VII. CONCLUDING REMARKS

The localized approximation introduced in the present work utilized a far reaching analogy between the electrically driven bending instability in the electrospinning process and the aerodynamically driven bending instability studied before.[2,4,5] The quasi-one-dimensional partial differential equations of the jet dynamics that describe the course of electrospinning were established. It was shown that the equations derived in Ref. 2 represent a discrete form of the partial differential equations derived in this article.

Based on the partial differential equations of the jet dynamics, the growth rate and the wavelength of the electrically driven bending perturbations of a viscous liquid column were calculated and the conditions characterizing the onset of such perturbations were elucidated.

In Ref. 2 the bending instability of jets in electrospinning responsible for the formation of nanofibers was explained as a particular case of a very general basic instability of a system of charged particles corresponding to Earnshaw's theorem. The quantitative description of Ref. 2, however, lacked the effects of solvent evaporation and solidification of the polymer jets leading to formation of dry nanofibers. In the present work a description of the evaporation and solidification was added to the model of Ref. 2. As a result, a reasonably quantitative description of the experimental data was achieved, which allowed us to calculate the shape of the envelope cone which surrounds the bending loops of the jet in the course of electrospinning. Also, the downward velocity of the jet can be calculated to be within an order of magnitude of the observed velocity. The theoretical results also allow for the calculation of the elongation of material elements of the jet. The calculated results also illustrate the increase in viscosity of segments of the jet as the solvent evaporates during the course of electrospinning.

It is emphasized that presently, information on the rheological behavior of polymer solution being elongated at the rate and other conditions encountered during electrospinning is rather scarce. Data on evaporation and solidification of polymer solutions in the electrospinning process are practically unavailable. Therefore at present a number of the parameters in this calculation can only be estimated by the order of magnitude, or found from experimental observations of the electrospinning process. Material science data acquired for the electrospinning process will allow researchers to avoid such obstacles in future. Also, a more detailed description of the nature of the solvent (in this case, mixture of water and ethanol with a variable evaporation rate) may be very helpful for a further upgrading of the present model.

[1] D. H. Reneker and I. Chun, Nanotechnology **7**, 216 (1996).
[2] D. H. Reneker, A. L. Yarin, H. Fong, and S. Koombhongse, J. Appl. Phys. **87**, 4531 (2000).
[3] G. I. Taylor, Proc. R. Soc. London, Ser. A **313**, 453 (1969).
[4] V. M. Entov and A. L. Yarin, J. Fluid Mech. **140**, 91 (1984).
[5] A. L. Yarin, *Free Liquid Jets and Films: Hydrodynamics and Rheology* (Longman, Harlow, and Wiley, New York, 1993).
[6] R. J. Arms and F. R. Hama, Phys. Fluids **8**, 553 (1965).
[7] G. K. Batchelor, *An Introduction to Fluid Dynamics* (Cambridge University Press, Cambridge, 1967).
[8] H. Aref and E. P. Flinchem, J. Fluid Mech. **148**, 477 (1984).
[9] A. L. Yarin, J. Non-Newtonian Fluid Mech. **69**, 137 (1997).
[10] C. Pozrikidis, *Introduction to Theoretical and Computational Fluid Dynamics* (Oxford University Press, New York, 1997).
[11] M. Stelter, G. Brenn, A. L. Yarin, R. P. Singh, and F. Durst, J. Rheol. **44**, 595 (2000).
[12] A. Ziabicki, *Fundamentals of Fibre Formation* (Wiley, London, 1976).
[13] M. Seaver, A. Galloway, and T. J. Manuccia, Rev. Sci. Instrum. **60**, 3452 (1989).